Natural Resources Canada | Ressources naturelles Canada

GEOLOGICAL SURVEY OF CANADA
OPEN FILE 8895

Exploring the link between organic matter and Carlin-type gold mineralization: new insights from Yukon deposits

N. Pinet, O.H. Ardakani, J. Cesar, D.C. Petts, C. Debuhr, and P.J. Sack

2022

Canada

GEOLOGICAL SURVEY OF CANADA
OPEN FILE 8895

Exploring the link between organic matter and Carlin-type gold mineralization: new insights from Yukon deposits

N. Pinet[1], O.H. Ardakani[2,4], J. Cesar[2], D.C. Petts[3], C. Debuhr[4], and P.J. Sack[5]

[1]Geological Survey of Canada, 490, rue de la Couronne, Québec, Quebec
[2]Geological Survey of Canada, 3303-33rd Street N.W., Calgary, Alberta
[3]Geological Survey of Canada, 601 Booth Street, Ottawa, Ontario
[4]Department of Geoscience, University of Calgary, 844 Campus Place N.W., 2500 University Drive N.W., Calgary, Alberta
[5]Yukon Geological Survey, 91807 Alaska Highway, Whitehorse, Yukon

2022

Permanent link: https://doi.org/10.4095/330086

This publication is available for free download through GEOSCAN (https://geoscan.nrcan.gc.ca/).

Recommended citation

Pinet, N., Ardakani, O.H., Cesar, J., Petts, D.C., DeBuhr, C., and Sack, P.J., 2022. Exploring the link between organic matter and Carlin-type gold mineralization: new insights from Yukon deposits; Geological Survey of Canada, Open File 8895, 22 p. https://doi.org/10.4095/330086

Publications in this series have not been edited; they are released as submitted by the author.

Exploring the link between organic matter and Carlin-type gold mineralization: new insights from Yukon deposits

Nicolas Pinet[1], Omid Haeri-Ardakani[2,4], Jaime Cesar[2], Duane Pett[3], Christopher Debuhr[4], Patrick Sack[5]

[1] Natural Resources Canada, Geological Survey of Canada, 490 Rue de la Couronne, Québec, QC G1K 9A9
[2] Natural Resources Canada, Geological Survey of Canada, 3303 33 Sreet NW, Calgary, Alberta, T2L 2A7
[3] Natural Resources Canada, Geological Survey of Canada, 601 Booth Street, Ottawa, Ontario, K1A 0E8
[4] University of Calgary, 844 Campus Place N.W., 2500 University Drive NW, Calgary, Alberta, T2N 1N4

[5] Yukon Geological Survey, 91807 Alaska Highway, Whitehorse, Yukon, Y1A 5B7

ABSTRACT

The link between organic matter and gold in sediment-hosted Carlin-type deposits is controversial. This study aims to tackle this potential link by documenting the occurrence of organic matter in a single borehole from a Carlin-type gold deposit in Yukon and by considering, in a preliminary way, the spatial and/or temporal relationship between organic matter and gold mineralization. The sedimentary succession hosting the Conrad deposit was relatively rich in organic matter, possibly related to Archea. Despite the high maturation of samples, the total organic carbon (TOC) content of the limestone unit averages 1.31 wt. % (maximum = 3.18 wt. %). Petrographic observations indicate that pore and fracture filling pyrobitumen is the dominant organic matter maceral in the studied samples. This type of pyrobitumen was matured after its emplacement, indicating that hydrocarbon fluids cannot have served as an agent for gold transport. Pyrobitumen disseminated in the rock or associated with stylolites are also documented. The correlation between TOC and Tl (the best proxy for Au) for selected samples and the high As content of pyrobitumen filling pores may suggest a link between organic matter content and gold deposition, but this was not demonstrated by LA-ICP-MS micro-scale mapping. This study also highlights the challenges of establishing a direct spatial relationship between 'invisible' gold and very small (< 10 μm) pyrobitumen particles.

INTRODUCTION

Carlin-type deposits are a major contributor to the global gold production and occur in sedimentary basins with surface maturation levels ranging from mature (i.e., within the oil window) to overmature (dry gas zone, maximum paleotemperature from less than 100°C to more than 200°C; Cline et al., 2005; Muntean, 2018). In the type localities of Nevada, the spatial relationship between carbonaceous sedimentary rocks and gold ore deposits have long been documented, but there are still contradictory views on the potential role of organic matter-rich

rocks on pre-mineralization gold enrichment, gold transport and gold concentration (Large et al., 2011; Muntean et al., 2011). In such settings, hydrocarbon generation and migration are generally interpreted to predate fluid influx associated with giant gold mineralization (Ilchick et al., 1986) and there is no correlation between ore grade and organic carbon in the host rock (Hofstra and Cline, 2000). However, at district to deposit scales, carbonaceous rocks may have been important in keeping fluids reduced which enhanced gold transport by sulfide complexes (Hofstra and Cline, 2000, Muntean, 2018). In other cases, evidence such as oil-bearing fluid inclusions in ore samples from the low-temperature end-member Carlin-type Alligator ridge district, suggest that hydrocarbons were introduced contemporaneously with gold (Hulen and Collister, 1999) and that hydrocarbons possibly served as a transport agent for gold (Williams-Jones et al., 2009; Large et al., 2011).

This study aims to document the spatial and/or temporal relationship between organic matter and Carlin-type gold mineralization in Yukon (Canada), and to test the hypothesis of an active role by the organic matter on the fertility of gold systems. Focus is placed on the nature of kerogen/bitumen (in situ or migrated), on the association with pyrite and on the chemistry of bitumen grains at the mm to µm scale. To reach this aim, detailed petrography is used to constrain paragenetic relationships. It is complemented by the organic geochemistry and the analysis of the total organic carbon (TOC) content through programmed pyrolysis analyses, detailed whole-rock geochemistry to investigate gold and pathfinder elements content, and scanning electron microscopy and energy dispersive X-ray spectroscopy (SEM-EDS) and laser ablation inductively coupled plasma mass spectrometry (LA-ICP-MS) mapping to reveal the distribution of gold and organic matter. The ultimate goal is to answer basic questions such as: a) Can bitumen be entrained by hydrothermal fluids? b) Can hydrocarbons be a transport agent for gold? and c) Can organic matter act as a reducing agent and enhance gold transport*?* Answers to these questions have direct implications for exploration as the characterization of the relationship between organic matter and gold may help pinpoint specific areas of the sedimentary succession.

CARLIN-TYPE MINERALIZATION IN YUKON

Sediment-hosted Au-bearing deposits in the central Yukon (Canada) are among the few examples of Carlin-type Au mineralization documented outside Nevada (Tucker et al., 2018; Pinet et al., 2022a). These deposits have been the focus of several recent studies, including a review of the regional to prospect scale setting of mineralized zones (Tucker, 2015; Steiner et al., 2018; Pinet et al., 2020a and 2022a), detailed descriptions of mineralized intervals (Tucker, 2015; Beaton, 2015; Pinet and Sack, 2019; Pinet et al., 2020b), whole rock and stable isotope geochemistry (Tucker, 2015; Beaton, 2015; Steiner and Hickey, 2019; Pinet et al., 2021 and 2022a), U-Pb dating of calcite associated with the late stage of the Au-mineralizing event (Pinet et al., 2022b), time-temperature frame of the deposits (Pinet et al., submitted) and a detailed characterization of Au-bearing pyrite (Sack et al., 2019 and in prep.).

In central Yukon, Carlin-type deposits are mainly hosted by Neoproterozoic limestone (with few mineralized intervals in siltstone) deposited in slope to base of slope settings (Nadaleen and Gametrail formations belonging to the Windermere Supergroup; Moynihan et al., 2019) and in mid-Paleozoic calcareous siltstones. In the Neoproterozoic-hosted Conrad and Sunrise/Osiris/Ibis deposits, Au mineralization is roughly concordant with bedding and occurs in stratigraphic and/or structural traps sealed by less permeable units. Mineralization is mainly hosted in carbonate floatstone and grainstone intervals interpreted to have formed through debris flow, and in highly fractured sedimentary units. Most fractures and veins predate mineralization, but some are syn- to late mineralization (Tucker et al., 2018; Pinet and Sack, 2019; Pinet et al., 2020a, b).

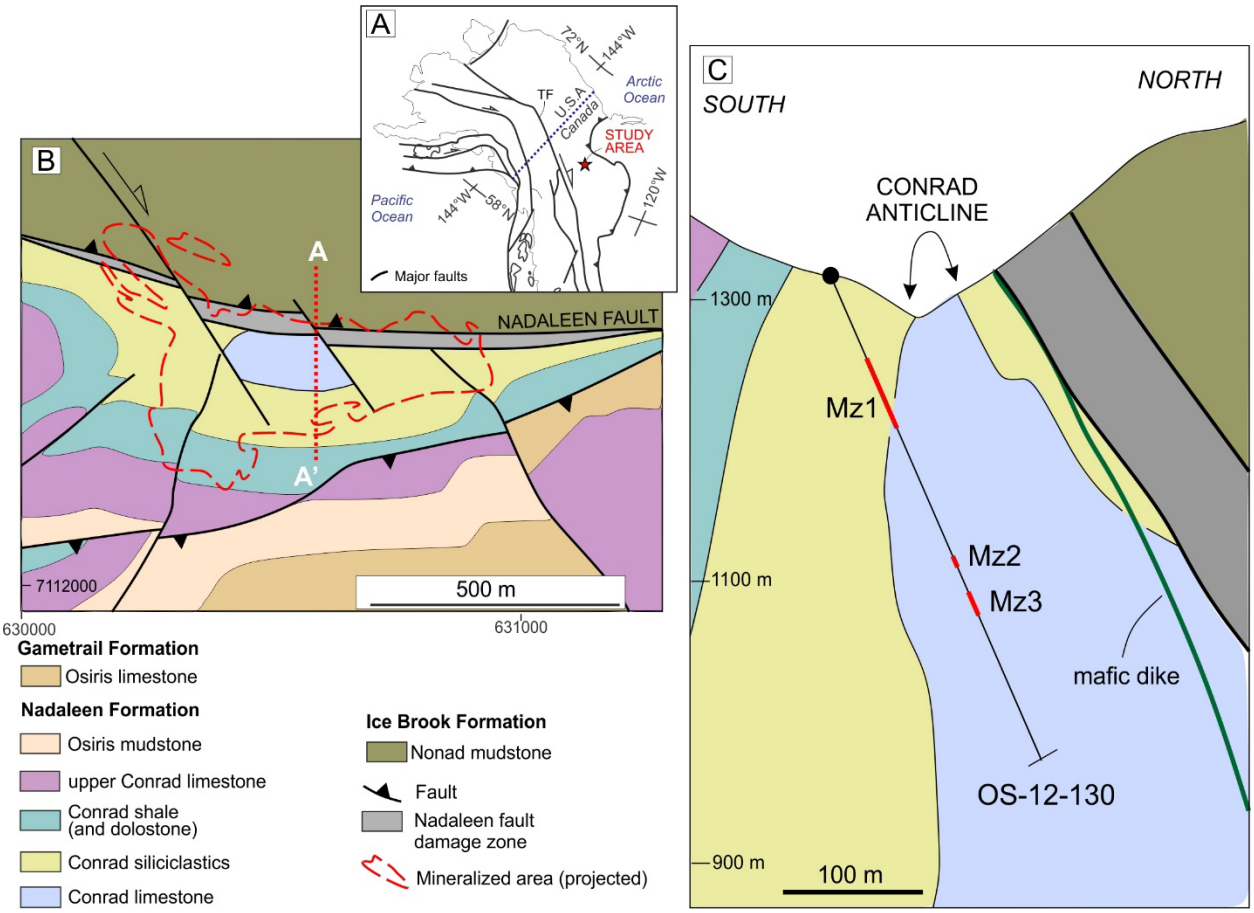

Figure 1. Geological setting of Carlin-type deposits in Yukon. A) Location of the study area. TF, Tintina Fault. B) Geological map of the Conrad deposit (modified from ATAC Resources unpublished maps and Steiner et al., 2018). Mineralized area from Ristorcelli et al., 2018. C) Cross-section of the Conrad deposit (A-A' on Fig. 1A) showing the location of borehole OS-12-130. Mz1, Mz2 and Mz3 refer to mineralized zones shown on Figure 2.

Partial to complete decalcification within mineralized intervals and silicification are the main alteration types, whereas argillitization is local and generally difficult to identify (Tucker, 2015; Pinet et al., 2022a). Gold occurs within thin arsenian pyrite rims (e.g., ~ < 10 µm) on pre-ore pyrite or as micron-scale particles in decalcified matrix (Sack et al., 2019). Whole rock chemical analyses indicate that Au is associated with pathfinder elements such as Tl, As, Hg, Sb and that base metal and Ag contents are low (Tucker, 2015; Beaton, 2015; Pinet et al., 2022a). U-Pb dating of zircon from an Au-mineralized dyke (Tucker, 2015) and of late-ore stage calcite associated with realgar (Pinet et al., 2022b) constrain the age of mineralization at *ca.* 74 Ma.

SAMPLING SUITE

This study is based on the detailed study of a single, 374 m long, borehole (OS-12-130) representative of the Conrad gold zone. The core from this borehole is stored at the Yukon Geological Survey (YGS) core facility in Whitehorse.

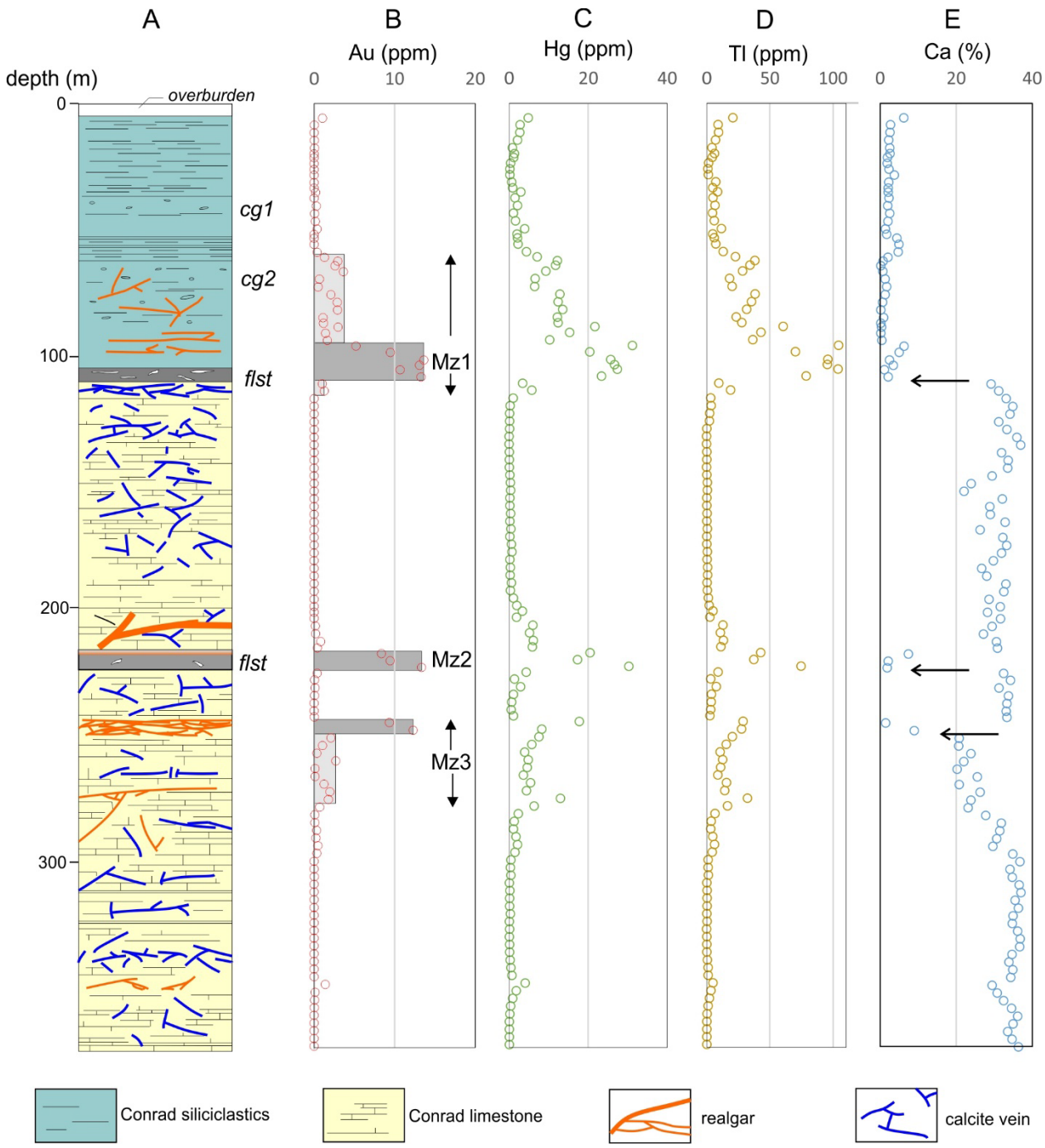

Figure 2. Lithological and main geochemical characteristics of borehole OS-12-130. A) Lithological column. Note the variable realgar content and the occurrence of floatstone intervals (flst) including one at the contact between the Conrad siliciclastics and the Conrad limestone. cg1 and cg2 are conglomerate intervals. B) Au content (from ATAC Resources database). Mz1, Mz2 and Mz3 are the three mineralized intervals (dark grey > 5 ppm Au; light grey < 5 ppm Au). C), D) and E) Hg, Tl and Ca contents (from ATAC Resources database). Note the high Hg and Tl values and the low Ca content (arrows) in Au-mineralized zones.

Borehole OS-12-130 is located on the southern flank of the Conrad anticline (Fig. 1). It dips *ca*. 67° toward the north and cuts successively the Conrad siliciclastics and the Conrad limestone of the Nadaleen Formation (Moynihan et al., 2019). In the upper part of the borehole (from 4.6 to 104.05 m; Fig. 2), the Conrad siliciclastics correspond mainly to a non calcareous laminated dark grey siltstone (with a few sandy intervals) and to two matrix-supported conglomerate intervals with apparent thickness of *ca.* 16 and 26 m. Conglomerates are in gradational contact with finer siliciclastic rocks and correspond to sub-rounded to sub-angular quartz fragments (*ca*. 30%), generally less than 1 cm in length within a siltstone matrix (*ca*. 70%). Pyrite (locally > 2 vol.%) is disseminated throughout the unit. Close to the contact with the underlying Conrad limestone, a few calcareous layers occur in the Conrad siliciclastics, indicating a gradational contact.

The contact between the Conrad siliciclastics and the Conrad limestone is marked by a 5.5 m (i.e.; *ca*. 2.15 m true thickness) dark grey to black floatstone interval (Fig. 2). Floatstone (following the original limestone classification of Dunham, 1962, modified by Embry and Klovan, 1971) corresponds to a matrix-supported sedimentary breccia with angular fragments of lime mudstone with no clear preferential orientation and interpreted as debris flow deposits formed on a carbonate slope (Pinet et al., 2022a). The floatstone has a low Ca content (*ca*. 2%; Fig. 2E) and does not react to diluted HCl, but its original carbonate content may have been much higher, as the interval is strongly decarbonatized.

The lower part of the borehole consists mainly of a medium grey, with some dark grey, lime mudstone/wackestone with some intraclastic packstone (and minor grey to black calcareous siltstone) and one floatstone interval. Limestone beds are generally from a few millimetres to 30 cm in thickness, and exhibit planar contacts. Fibrous calcite veins (beef and cone-in-cone textures) are observed at several levels and may have formed as hydraulic fractures through degassing of biogenic methane during shallow burial (Meng et al., 2017), suggesting that the sediments were originally rich in organic-matter. Calcite veining is present throughout the limestone interval and vary from 3 to >30%. Several generations of stylolite either parallel to or discordant with bedding are documented.

Three high-grade (> 5 ppm Au) mineralized intervals occur within borehole OS-12-130. The upper mineralized interval (Mz1 on Fig. 2) is located at the contact between the Conrad siliciclastic and underlying Conrad limestone. The highest grade zone (11.05 ppm Au over 14.64 m) in Mz1 is found in the lower part of the Conrad siliciclastic unit and in the floatstone interval (Fig. 3A) and is bounded on both sides by lower grade zones composing a 54.86 m (apparent thickness) interval grading 4.32 ppm Au. Realgar-rich veins either parallel or discordant to bedding occur locally (< 3%) in the mineralized interval. The second mineralized interval (216.3 to 224.1 m depth) yields 10.21 ppm Au over 7.8 m (Mz2 on Fig. 2). It corresponds to a black, almost featureless interval with a few angular sedimentary fragments and is interpreted as a matrix-rich floatstone interval. This interval shows no reaction to diluted HCl, due to intense decarbonatization. The lower mineralized interval (Mz3 on Fig. 2) includes an orange color high-grade zone (10.88 ppm Au over 5.9 m; i.e. between 243.4 to 249.3 m) characterized by anastomosed sets of realgar veins that give to this interval a brecciated aspect (Fig. 3B). Below the high-grade zone, a lower grade interval in Mz3 (1.28 ppm Au over 27.4 m; i.e. between 249.3 to 276.8 m) is characterized by lesser amounts of realgar.

METHODS

Ninety-eight samples taken at sampling intervals between < 1 m and 10 m were collected in borehole OS-12-130 for programmed pyrolysis (HAWK TOC analyzer), organic petrography and geochemistry, and elemental analyses. These samples were selected on the basis of their medium grey to black color suggesting higher organic matter content than surrounding rocks. An additional 4 samples were collected from carbonate intervals with stylolite in both low and high-grade intervals.

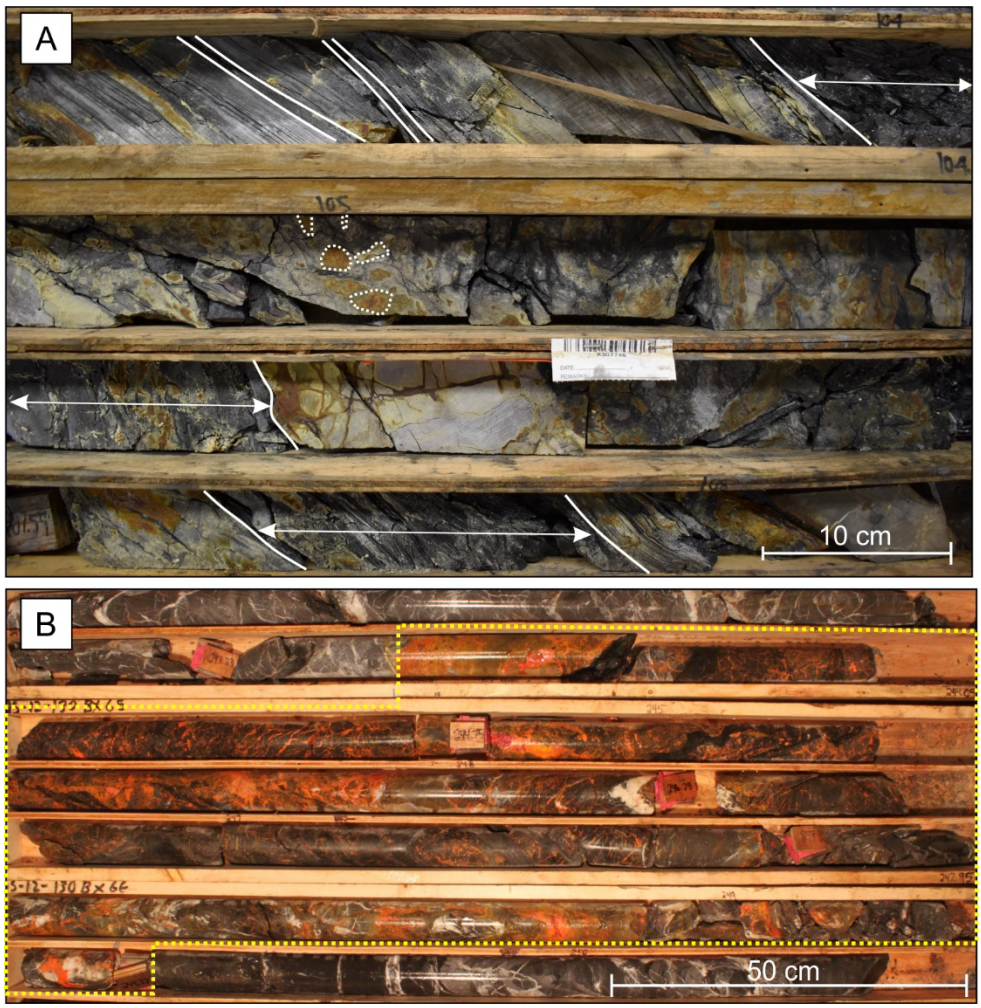

Figure 3. Pictures of mineralized intervals Mz1 and Mz3 (courtesy of ATAC Resources). A) Decarbonatized Mz1 interval including alternating fine grained rocks (originally lime mudstone?) and a floatstone interval (some fragments outlined by white dashed lines). Arrows indicate darker intervals that suggest high organic content. B) Realgar-rich mineralized interval Mz2. The yellow dotted box outlined an interval yielding 10.88 ppm Au over 5.9 m.

Geochemistry

The geochemical signature of mineralization and alteration in borehole OS-12-130 was investigated using data from the ATAC Resources database and new whole-rock analyses on selected samples. Analyses from the ATAC Resources database comprised 131 analyses for 50 elements, not including silica (Si). The average length of the assayed intervals is 2.82 m. Analytical method is available in Pinet et al. (2021). Nineteen (19) new whole-rock analyses were performed as part of this study. The bulk composition of major, minor and trace elements were determined using ICP-MS at Acme Laboratories in Vancouver, and data quality was checked by international standards and analysis of replicate samples (analytical precision and accuracy are within 10% for all samples). Samples were digested using a combination of high purity acids (HF, HNO_3, $HClO_4$, HCl)

Programmed pyrolysis

Bulk samples (n = 98) were analyzed through programmed temperature heating by HAWK pyrolysis to document the total organic carbon (TOC) content (Lafargue et al., 1998). Interpretation of the maturity indicator Tmax for the same dataset is reported in Pinet et al. (submitted). HAWK pyrolysis consists of programmed heating of a small amount of powdered rock (~ 70 mg) to determine the quantity of free hydrocarbons present in the sample (S1 peak) and the amount of hydrocarbons and oxygen-containing compounds (CO_2) that are produced during the thermal cracking of the insoluble organic matter (kerogen) in the rock (S2 and S3CO_2 peaks respectively).

The pyrolysis stage (under N_2 environment) involved the initial iso-temperature of 300°C for 3 min to release free hydrocarbons in the samples (S1, mg HC/g rock). This step is followed by a ramping temperature of 25°C/min up to 650°C to release hydrocarbons and the oxygen contained in pyrolizable kerogen (S2, mg HC/g rock, and S3, mg CO_2/g rock, respectively) through thermal cracking. Samples were then automatically transferred to the oxidation oven and heated from 300°C to 850°C with the heating rate of 20°C per minute to measure the residual inert organic carbon (S4, mg CO and CO_2/g rock and residual carbon (RC) wt.%) and a portion of the mineral carbon (MinC, wt.%). Total organic carbon (TOC, wt. %) is quantified as the sum of the total quantity of OM released during pyrolysis (Pyrolizable Carbon, PC wt. %) and the oxidation step (RC wt. %). The oxygen index (OI) is calculated by normalizing the quantity of pyrolizable CO2 (S3) to total organic carbon (S3/TOC x 100) and is proportional to the elemental O/C ratio of the kerogen. The hydrogen index (HI) corresponds to the ratio S2/TOC x 100 and is proportional to H/C (Lafargue et al., 1998).

Organic petrography

Twelve (12) samples from low- and high-grade zones were selected for organic petrography. Organic petrography was carried out using polished blocks made with a cold-setting epoxy–resin mixture. The resulting sample pellets were ground and polished in preparation for microscopy, using an incident light Zeiss Axioimager II microscope system equipped with an ultraviolet (UV) light source and the Diskus-Fossil system. Fluorescence microscopy of OM was carried out using UV G 365 nm excitation with a 420 nm barrier filter. Bitumen reflectance (%BRo) measurements on these samples are reported by Pinet et al. (submitted).

Organic geochemistry

A total of 6 samples were selected for molecular analysis. The organic fractions were extracted using a soxhlet apparatus for 24 hours. The total bitumen extracts were analyzed using gas chromatography quadrupole-time-of-flight mass spectrometry (GC-QToF-MS). The analysis was performed in an Agilent GC-QTOF 7200 equipped with a 60m DB5ms (0.25mm x 0.25um) capillary column, with a 1:10 split injection and helium as the carrier gas. The initial temperature of the GC oven was 40°C and then ramped to 325°C at 4°C/min to be held isothermally for 15 min. The samples were selected based on the pyrolysis data, i.e. total organic carbon and estimated free hydrocarbons (S1 peak) in the samples.

Scanning Electron Microscopy Energy Dispersive X-ray Spectroscopy (SEM-EDS)

One thin section with a well-defined stylolite and one organic petrography sample (‘pellet’) were selected for field emission scanning electron microscope (SEM) imaging and energy-dispersive X-ray spectroscopy (EDS) in order to quantify the inorganic fraction of the rock and the distribution of organic matter particles in the rock matrix. Analyses of the organic petrography sample were undertaken on 5 zones. This work was conducted at the University of Calgary's Instrumentation Facility for Analytical Electron Microscopy using the FEI Quanta 250 FESEM under low vacuum conditions.

The first of the studied samples includes a *ca*. 2 mm thick stylolite (depth = 237.2 m), and has low As and Tl whole-rock values (respectively 58 and 10 ppm) suggesting very low-grade mineralization, but was chosen for SEM analysis with the hypothesis that mineralization is confined to the stylolite itself. The second studied sample is an organic petrography sample that was acquired from a depth of 245.2 m. It is characterized by a relatively high TOC of 1.78 %. The sample is significantly enriched in As and Tl (4,745 and 90.1 ppm respectively). Based on the relationship between Tl and Au for the Conrad limestone (Tl = 5.18 Au + 3.91; R^2 = 0.62), this suggests high-grade (> 5 ppm Au) mineralization.

LA-ICP-MS

The organic petrography sample studied through SEM-EDS was analyzed using LA-ICP-MS elemental mapping at the Geological Survey of Canada (Ottawa). Elemental mapping was undertaken using a Applied Spectra RESOlution-SE excimer laser ablation system (λ = 193 nm), with an S155 sample cell, coupled to an Agilent 7700x quadrupole ICP-MS. Elemental maps were constructed by translating a sample across a focused laser beam to form a series of line scan ablations. The analytical procedure closely followed the methods of Lawley et al. (2020) and Pinet et al. (2022b). Data were obtained over three sessions with analytical conditions consisting of: a spot size and laser scan speed of 7 µm @ 14 µm/s and 10 µm @ 20 µm/s; laser fluence and repetition rate of 4.5 J/cm^2 and 30/40 Hz, and carrier gas flows of ~ 0.5 L/min helium and 1.1 L/min argon.

RESULTS

Geochemistry

Whole rock geochemistry analyses of borehole OS-12-130 from the ATAC Resources database exhibit the typical geochemical characteristics documented in Yukon Carlin-type Au-deposits (Tucker, 2015; Pinet et al., 2022) and in most of Carlin-type deposits worldwide (Cline et al., 2005; Muntean, 2018). Tl and Hg show the best correlation with Au (Fig. 2; R^2 of 0.72 and 0.73, respectively). High-grade intervals have low (< 10 wt. %) Ca content indicating strong decarbonatization (Fig. 2), even if an originally low Ca content in the mineralized floatstone interval at the siliciclastic-limestone boundary cannot be ruled-out.

Major and trace element results from selected samples collected for this study are in overall agreement with analyses from the ATAC database and sampled mineralized zones 2 and 3 exhibit the classic pathfinder elements associated with Carlin-type mineralization, including high Tl values in Au-mineralized zones (Fig. 4B). This indicates that these analyses can be used for investigating the relationship between organic matter content (TOC) and mineralization (see discussion section below). Selected samples from mineralized zones 2 and 3 also have the lowest Ca concentration which can be associated with extensive acid leaching. Comparison of Tl content from core intervals averaging 2.8 m (ATAC Resources database) and selected medium grey to black samples indicates that the later have higher Tl (Fig. 5A), suggesting that they are more Au-mineralized. Al, which is an immobile element (Pinet et al., 2022a), is also significantly higher in selected samples (Fig. 5B) suggesting an initially higher Al content (i.e. rocks were more siliciclastic) than surrounding limestone, even if a potential volume loss that occurred during mineralization may have contributed to Al enrichment.

Programmed pyrolysis

The results of programmed pyrolysis analysis are presented in Pinet et al. (submitted). The total organic carbon (TOC) content ranges from 0.3 to 3.2 wt.% with a mean value of 1.1 ± 0.6 wt.% (n = 98). The first 100 m of the core is characterized by lower a TOC content compared to the rest of the core. The highest TOC contents are found in the lowest part of the borehole (Fig. 4C). The mean values of S1 (free hydrocarbon) and S2 (hydrocarbon potential/kerogen content) is equal to 0.06 ± 0.04 and 0.05 ± 0.04 mg HC/g, respectively (Pinet et al., submitted). Due to low S2 content, the Tmax (i.e., thermal maturity

proxy) varies from 289 to 608°C which is not reliable. The mean residual carbon to TOC ratio (0.97 ± 0.02) indicates almost complete conversion of organic matter. The mean hydrogen index (HI) and oxygen index (OI) of the samples are equal to 4.6 ± 4.1 mg HC/g TOC and 44 ± 28 mg CO_2/g TOC (Pinet et al., submitted). All values are representative of an overmature sample with high organic matter conversion rate.

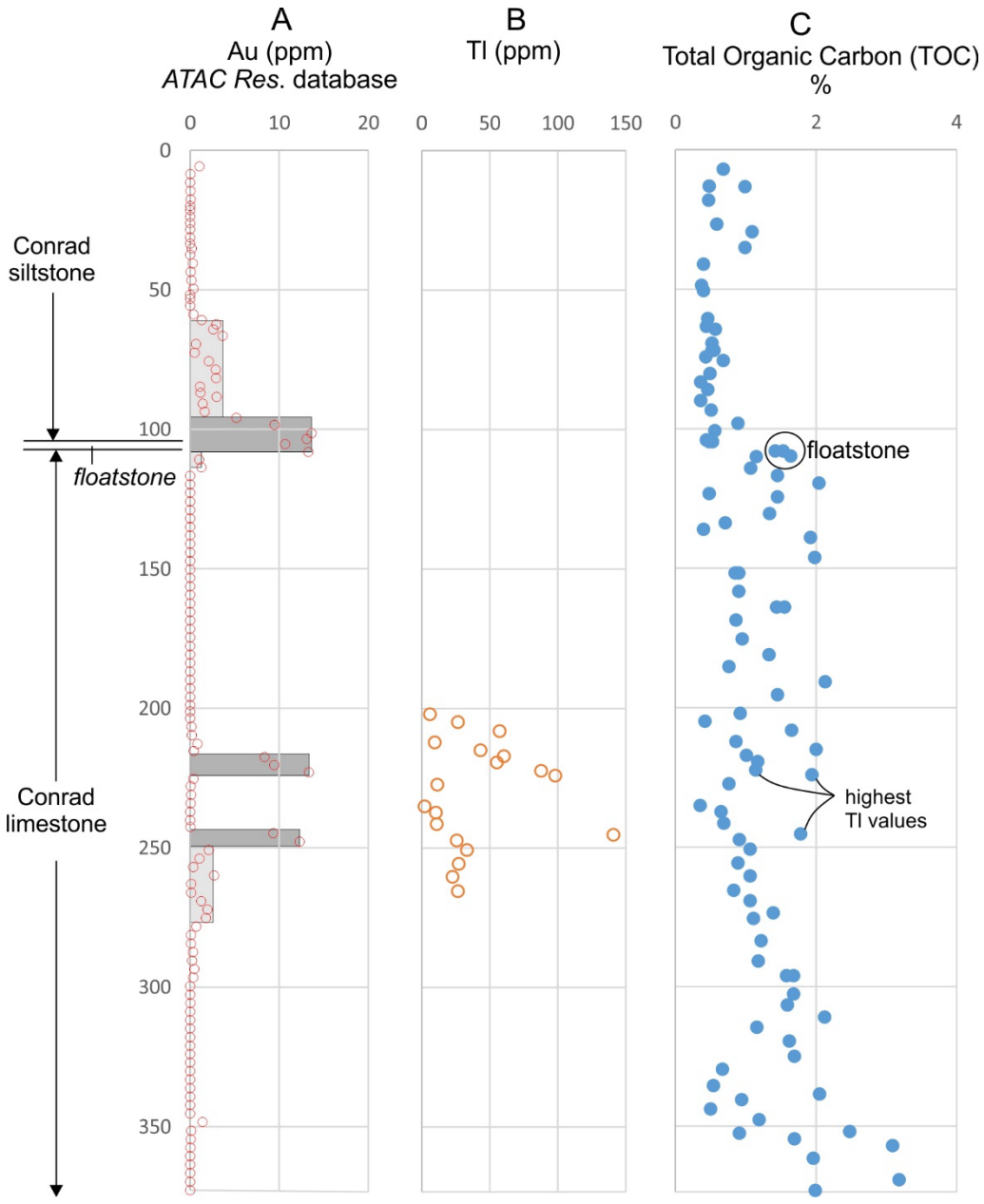

Figure 4. A) Au-mineralized zones (data from ATAC Resources database); B) Tl content of selected samples (this study). Tl is considered as the best proxy for Au. C) Total organic content of selected samples. Note the relatively high (> 1 wt. %) TOC values in high grade mineralized intervals.

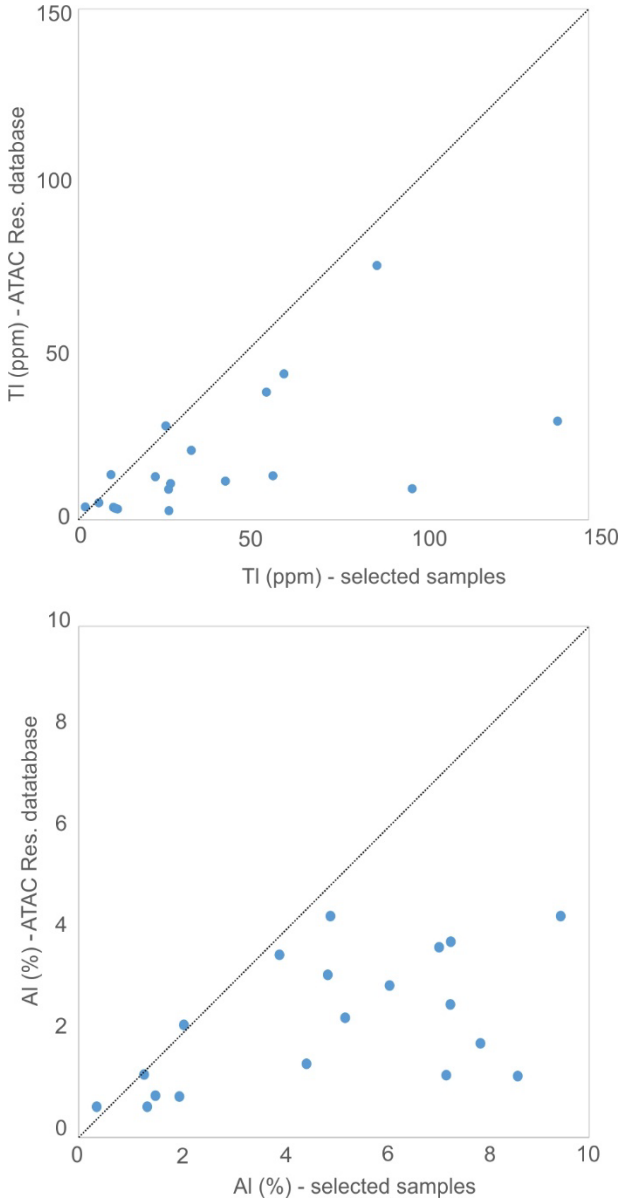

Figure 5. Comparison of ATAC Resources analyses (*ca*. 2.8 m long core) and analyses of selected samples collected for this study. A) Tl content; B) Al content. See text for comments.

Organic petrography

Pyrobitumen is the dominant organic matter maceral in the studied samples and is either disseminated in the rock, filling pores and fractures or associated with stylolites (Fig. 6). In the host organic-rich shale intervals, pyrobitumen occurs as thin laminae that resemble the shape of precursor algae transformed to pyrobitumen in situ or disseminated in the shale matrix (Fig. 6A-C). These organic-rich shaly facies are generally associated with the highest amount of pyrite (generally framboidal). Pore-filling or fracture filling textures are the major occurrence of pyrobitumen (Fig. 6B, H). Bitumen-filled pores have irregular shapes and range in size from 1 to 50 µm. In carbonate host rock, pyrobitumen is restricted to stylolites (Fig. 6F). In such samples pyrobitumen was a precursor liquid hydrocarbon phase that lined the stylolite walls (Fig. 6E) or filled the pores (within host limestone) and through thermal cracking transformed to pyrobitumen.

Petrographic observations and SEM-EDS

Petrographic observations and SEM images indicate that pyrobitumen-rich zones are associated with high concentration of pyrite with various morphologies (Fig. 7). Framboidal pyrite (Fig. 7A, B) is the predominant form of pyrite and range in size from > mm to < 10 µm. In some cases, specific morphologies are documented including: a) an assemblage of framboidal pyrite that fused together (Fig. 7A and 7F), b) an overgrowth 'corona' formed on the pyrite assemblage (Fig. 7C) and/or single framboidal pyrite and c) pyrite replacement of some other particles (Ediacaran fossil?; Fig. 7D). Pyrite with anhedral to euhedral morphology is also observed in the studied samples and, in some cases exhibit a narrow rim with a blocky texture (Fig. 7E). Such rims are generally Au-rich (Sack et al., 2019 and in prep.), but this was not verified in the analyzed samples.

SEM-EDS analyses of one organic petrography sample (245.2m, 073/21) and one stylolite thin section (237.2m) successfully characterized the Al, Fe, P, Si, S, Ti, ± As, Ca, C, K, Mg, Sr, but failed to map Au distribution. The lack of detectable gold prevents the study of a potential spatial association between organic matter and gold and suggests that analyzed zones in the two

studied samples were below detection limit for EDS for Au (~0.2 wt. % according to Wirth et al., 2013). This could be related to the difficulty to target Au-rich zones due to their similar appearance with Au-poor background, and to electron penetration depth that can be on the order of a few microns leading to X-ray spectra that may average the signals from both Au-rich nanoparticles and their host minerals. SEM-EDS images illustrate semi-quantitatively the distribution of carbon and confirm the three main modes of occurrence of bitumen: dispersed in the rock matrix (Fig. 8A, B), filling pores (Fig. 8C,D) and associated with stylolite (Fig. 8E, F).
Spectra from 5 pores filled with bitumen are presented on Figure 9. Arsenic is present in significant amounts in 4 of these spectra. As content is difficult to ascertain, but an estimate of several percent is probably a minimum.

LA-ICP-MS

LA-ICP-MS elemental maps of the organic petrography sample OS-12-130-245.2m clearly image Au-rich zones but cannot directly resolve C associated with pyrobitumen due to its occurrence as fine crystals (< 10 µm), which prevents a µm scale investigation of the spatial relationship between Au and C. Au values > 100 ppm are found in the three elemental maps of sample OS-130-245.2m, either as disseminated in the mapped area, located in an elongated zone (Fig. 10B) or concentrated in a ~ 1 mm long silicified zone.

Figure 10 shows one of the elemental maps and illustrates some of the difficulties to adequately map C-rich zones associated with pyrobitumen. SEM images indicate that pyrobitumen grains are generally finer than the spot size (7 µm; Fig. 10C) which result in a mixed signal between pyrobitumen and the host rock. Moreover, LA-ICP-MS is not an ideal instrument for quantifying carbon minerals at high resolution (i.e., <10-15 µm), and in our mapping work, the detection limit for carbon is in the range of 5-10%, which may be problematic for fine pyrobitumen crystals (i.e., smaller than the laser spot size) that result in mixed signals. Finally, the presence of nearby epoxy in the organic petrography sample can cause fluctuations in the background measurement of carbon, which results in apparent carbon variability in the sample matrix – a potential artifact unrelated to the occurrence pyrobitumen (Fig. 10A).

Organic geochemistry

Common hydrocarbon biomarkers such as hopanes, steranes, and *n*-alkanes were not found in the rock extracts. Their absence is anticipated due to the high thermal maturity of the rock (> 2.35 %BRo), which causes the organic matter to transform into highly aromatized structures that are insoluble in organic solvents (i.e. pyrobitumen as described by the organic petrography). However, after searching for different compound classes using their corresponding ions (*m/z*), some components were detected. They correspond to a series of branched alkanes, most of them with isoprenoid structure. Figure 11 illustrates the relative chromatographic distribution of these compounds and some of the structures identified using the mass spectra.

Figure 12 presents the fragmentograms of *m/z* 57 of all the samples to illustrate potential depth variations of the compounds detected. The *m/z* 57 trace corresponding to the extract blank or procedure blank is also shown, since it is important to identify possible sources of contamination. An extract blank or procedure blank corresponds to the solvent collected after the soxhlet extraction procedure where no sample was added. Figure 12 does confirm the presence of contaminants in the extract blank that could have been carried over in the samples. However, the majority of the contaminants do not correspond to the branched alkanes identified in the samples (many of the peaks do not have the same retention time). Although branched alkanes are regular constituents of all types of organic matter (e.g. all kerogen types) and petroleum samples routinely analyzed in the organic geochemistry laboratory, we would expect to find them accompanied by *n*-alkanes of similar molecular weight, but this was not the case. A source of contamination of exclusively branched alkanes seems rather unlikely.

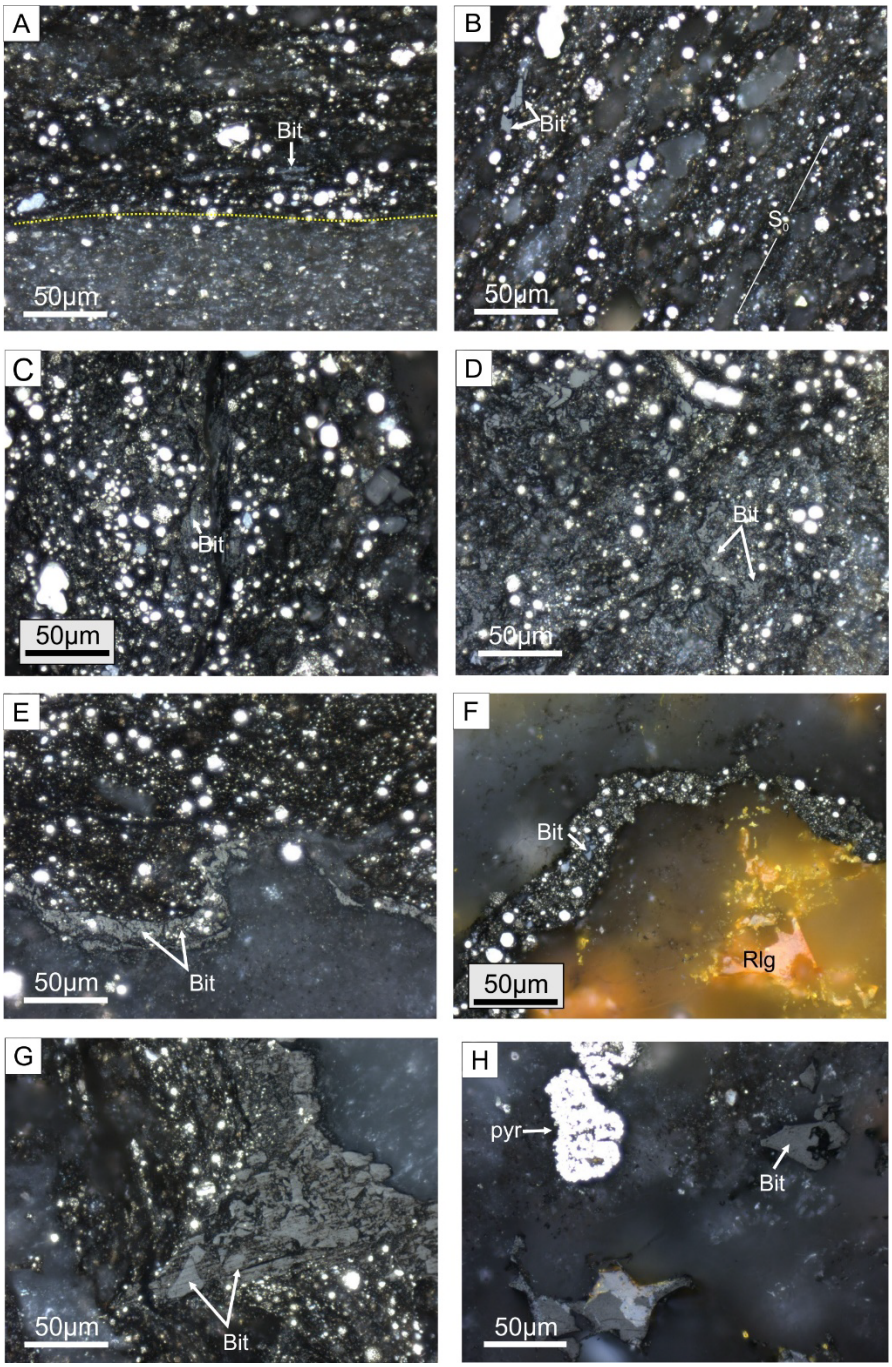

Figure 6. Organic petrography photomicrographs, all images were taken by incident white light with oil immersion ×50 objective. A) Boundary between barren host and fine-grained pyritic interval with filamentous pyrobitumen (351.9m). B) Interlamination of organic-rich and sand/silt with pore-filling pyrobitumen. The shale groundmass has disseminated organic matter (214.9m). S_0, bedding. C) Pyritic shale with filamentous pyrobitumen, likely bituminized algae, as well as pore-filling pyrobitumen (214.9m). D) Massive accumulation of pyrobitumen within stylolite, framboidal pyrite associated with pyrobitumen (245.2m). E) Boundary between organic-rich shale and host rock, pyrobitumen mainly accumulated at the boundary (190.7m). F) Stylolite formed between realgar and host rock filled with pyritic organic matter, pieces of pyrobitumen are floating in the clay-rich matrix within the stylolite (245.2m). G) Large accumulation of pyrobitumen within stylolite (237.2m). H) Accumulation of fused fine-crystalline pyrite in the host rock. Pores within the host rock filled with pyrobitumen (237.2 m).

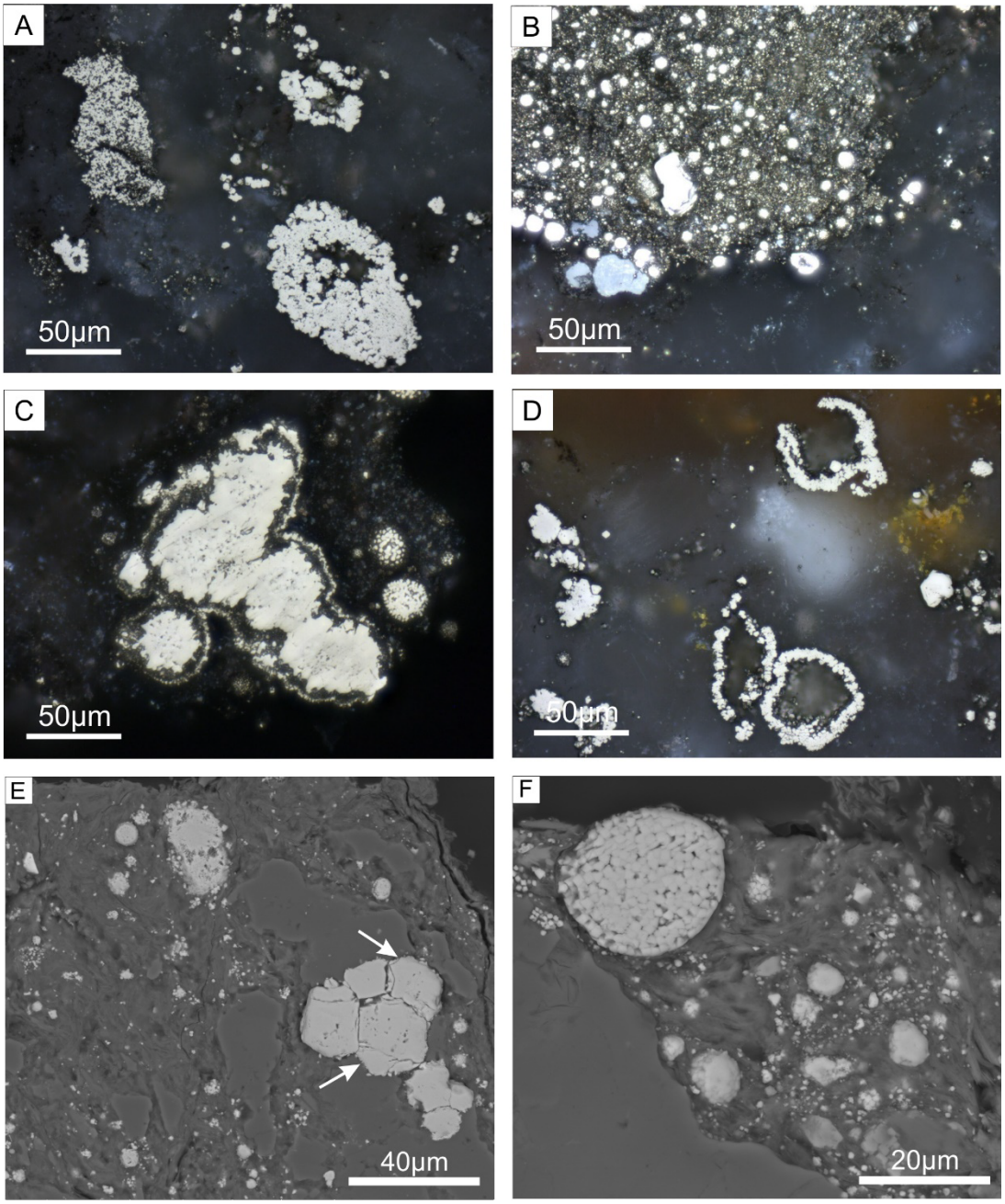

Figure 7. A) to D) Pyrite photomicrographs from stylolite sample at 237.2 m (low- Au interval). A) Accumulation of fine-crystalline pyrite, framboidal pyrite and framboidal pyrite fused together**.** B) highly pyritized organic matter matrix with fine-crystalline, framboidal and crystalline pyrite. C) Assemblage of framboidal pyrite, recrystallized fused with pyrite overgrowth. D) fine-crystalline pyrite replaced shell (?) fragments. E) and F) SEM images of pyrite forms in sample at 245.2 m (high-grade interval). E) fused framboidal and large crystalline pyrite. Note the 'blocky' rims (arrows) on euhedral pyrites. These rims are often Au-rich (Sack et al., 2019), but this was not demonstrated in this study. F) Large framboidal pyrite in association to smaller crystalline pyrite

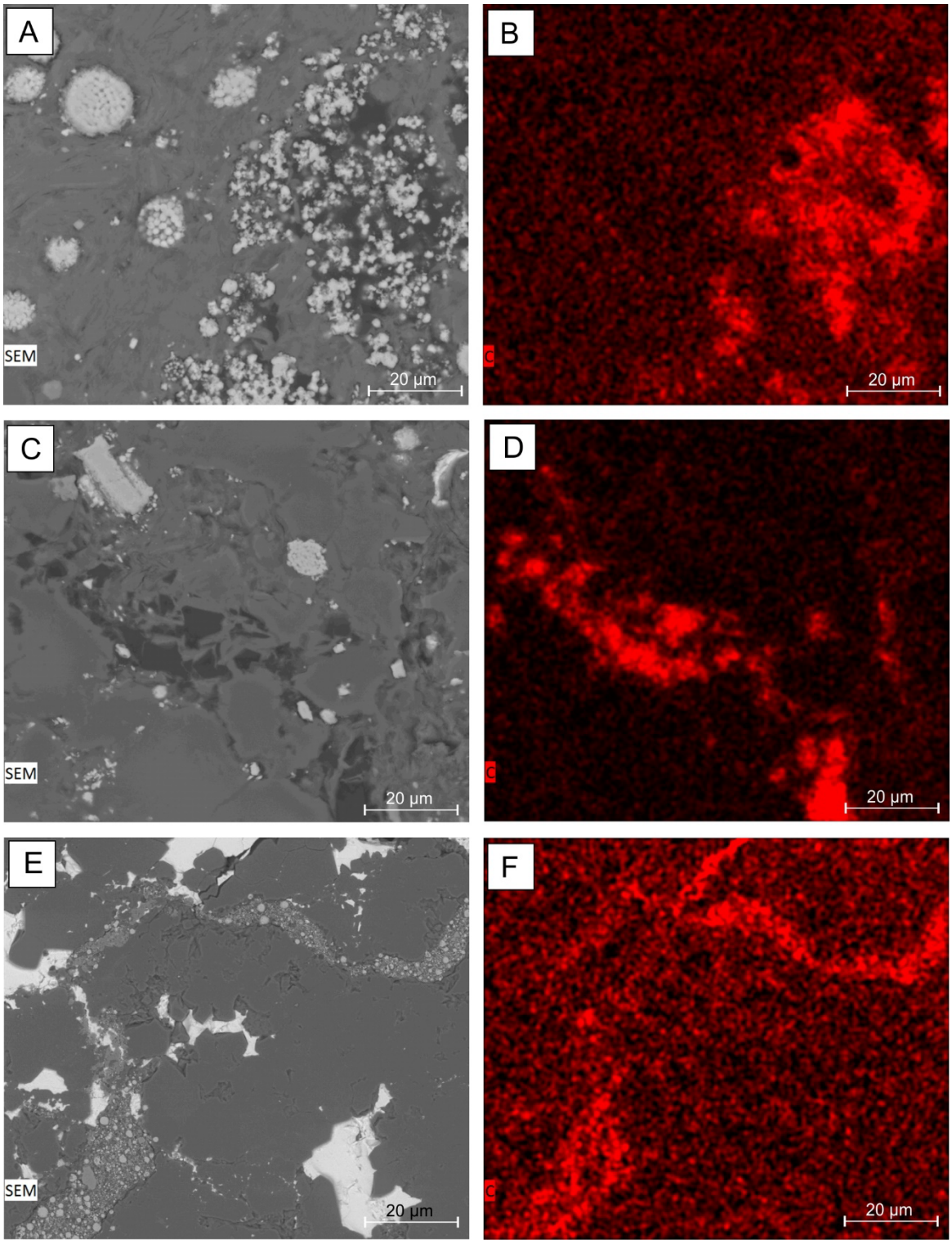

Figure 8. SEM images (A, C, E) and SEM/EDS maps for carbon (B, D, F) of organic petrography pellet at 245.2 m (high-grade zone). A) and B) irregular zone of disseminated organic matter rich with fine-grained pyrite. B) and C) pore-filling organic matter (black spots) within a silica-rich host. E) and F) Organic matter associated with pyrite within a stylolite.

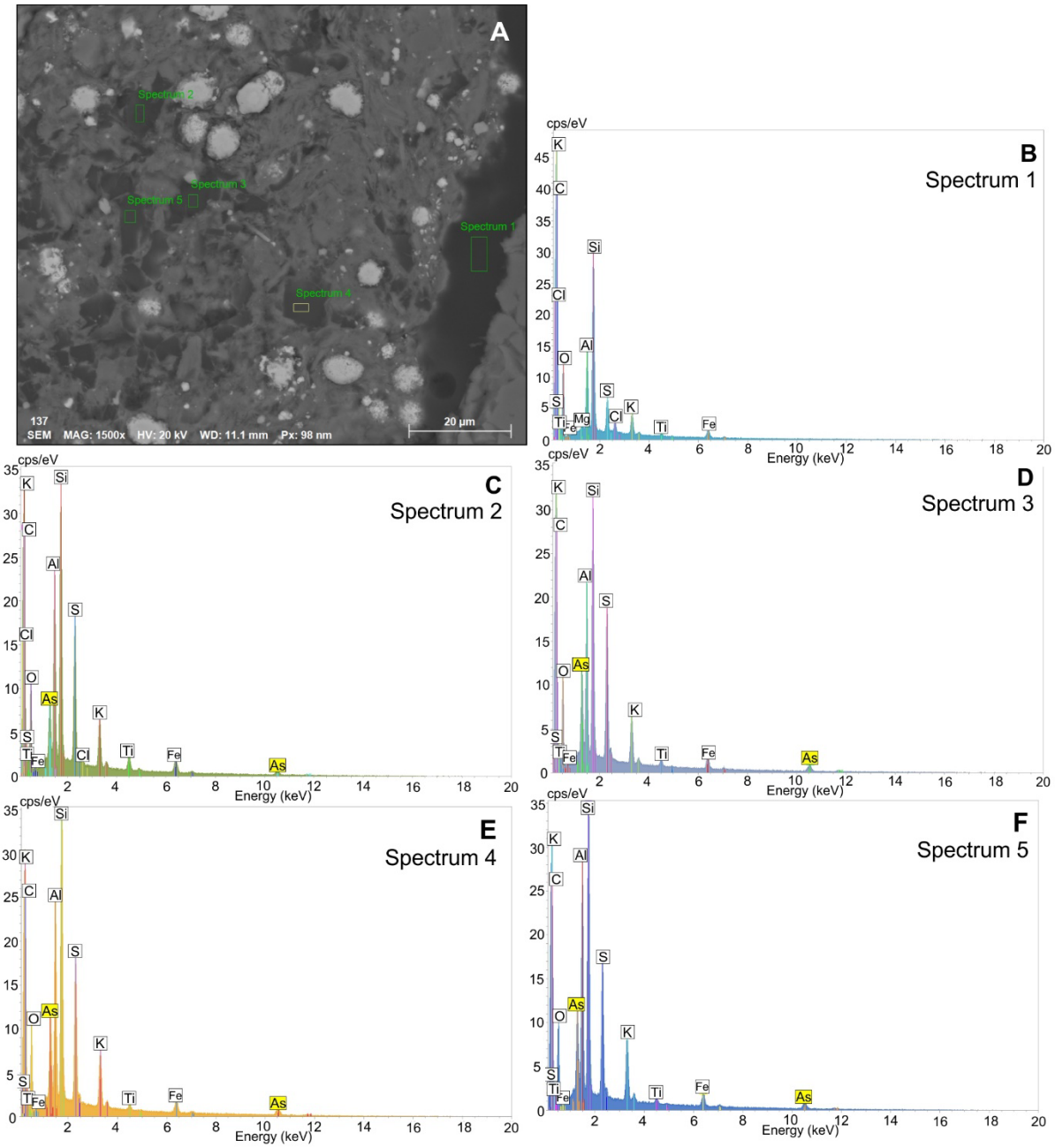

Figure 9. A) SEM image of organic petrography pellet at 245.2 m (high grade zone); B) to F) Spectra from 5 pores filled with bitumen. Note that As is present in significant amounts in 4 of these spectra.

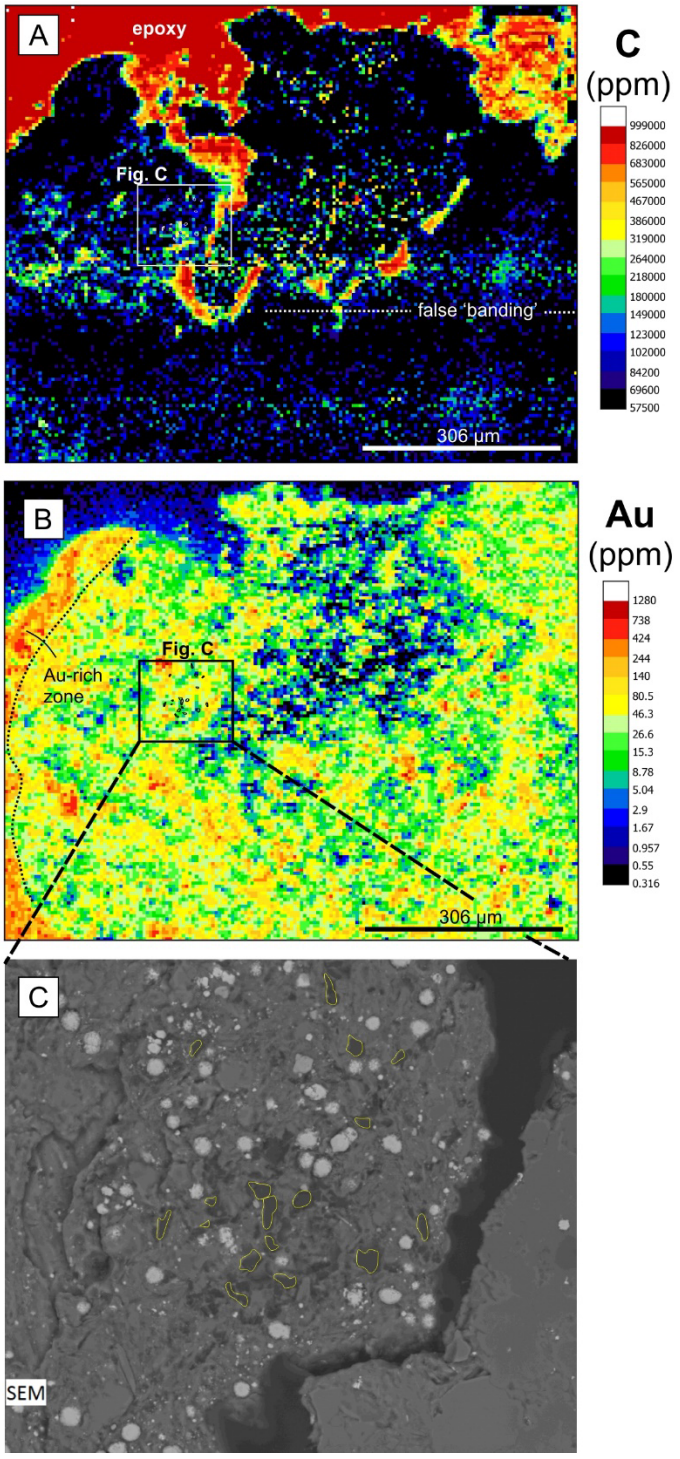

Figure 10. Elemental maps (A and B) and SEM image (C) for sample OS-12-130-245.2 m. Note the artifact (false 'banding') in A), the Au-rich zone in B) and the very fine size of pyrobitumen in C). Location of the SEM image in A) and B) is approximate and may be a few 10's µm apart.

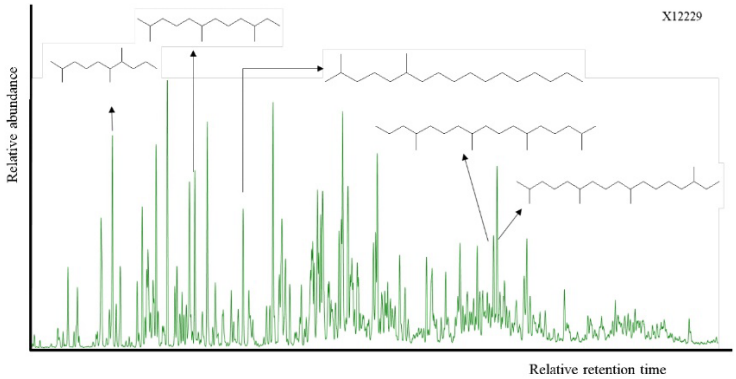

Figure 11. Fragmentogram of *m/z* 57 showing branched alkanes detected in the samples.

All fragmentograms show nearly similar compounds of higher molecular weight (compounds eluding later or right side of the fragmentograms). However, compounds of lower molecular weight (compounds eluting earlier or left side of the fragmentograms) are less abundant in two samples located at depths of 214.9 and 361.5 m. In the absence of reflectance data for these samples, thermal degradation (possibly linked with focussed hydrothermal fluid flows, associated or not with Au-mineralization) may be speculated as a possible reason for the degradation of lighter components. However, further analyses are required to explain variations in the molecular distribution.

DISCUSSION

Organic matter distribution

The limestone-unit hosting mineralization is characterized by relatively high TOC content averaging 1.31 wt. % (maximum = 3.18 wt. %) compared to TOC content in the siliciclastic unit (average = 0.57 wt. %; maximum = 1.09 wt. %). Considering the high maturation of these samples, the original organic matter content was significantly higher (Jarvie et al., 2007) and comparable to TOC values in some Phanerozoic hydrocarbon-prone basins. However, the organic geochemical data indicates that organic matter is possibly related to some type of archea (prokaryote) and not to eukaryotic organisms as in most Phanerozoic basins. Archea are diverse and abundant and not only in extreme environments as previously thought (Gribaldo and Brochier-Armanet, 2006) and preferentially synthesize high concentrations of biphytane and other long chain isoprenoids, such as those found in pyrobitumen. The presence of isoprenoids has already been documented in several sedimentary successions of the same age and older (e.g. Neoproterozoic and Archean). Further research is necessary to confirm the occurrence of these compounds. Hydro-pyrolysis experiments as well as strict protocols using multiple control blanks will enhance the reliability of the results.

Due to thermal alteration (Pinet et al., submitted), organic matter was transformed in pyrobitumen. Three morphologically different of pyrobitumen types were identified. The first type corresponds to dispersed matrix bitumen that appeared as fine-grained gray spots often associated with framboidal pyrite and disseminated in the matrix of rock, suggesting a 'self-source' reservoir (i.e, organic matter thermally matured *in situ* with almost no migration). Pyrobitumen found in pores and fractures is the most abundant and constitutes the second type. It corresponds to residues of liquid hydrocarbons that were generated some distance from the original source during a burial period when intrabasinal organic-shales passed progressively through the oil window at temperature of 100-150°C, migrated to their present location and were subsequently transformed to pyrobitumen. The third type of bitumen is associated with several generations of stylolites.

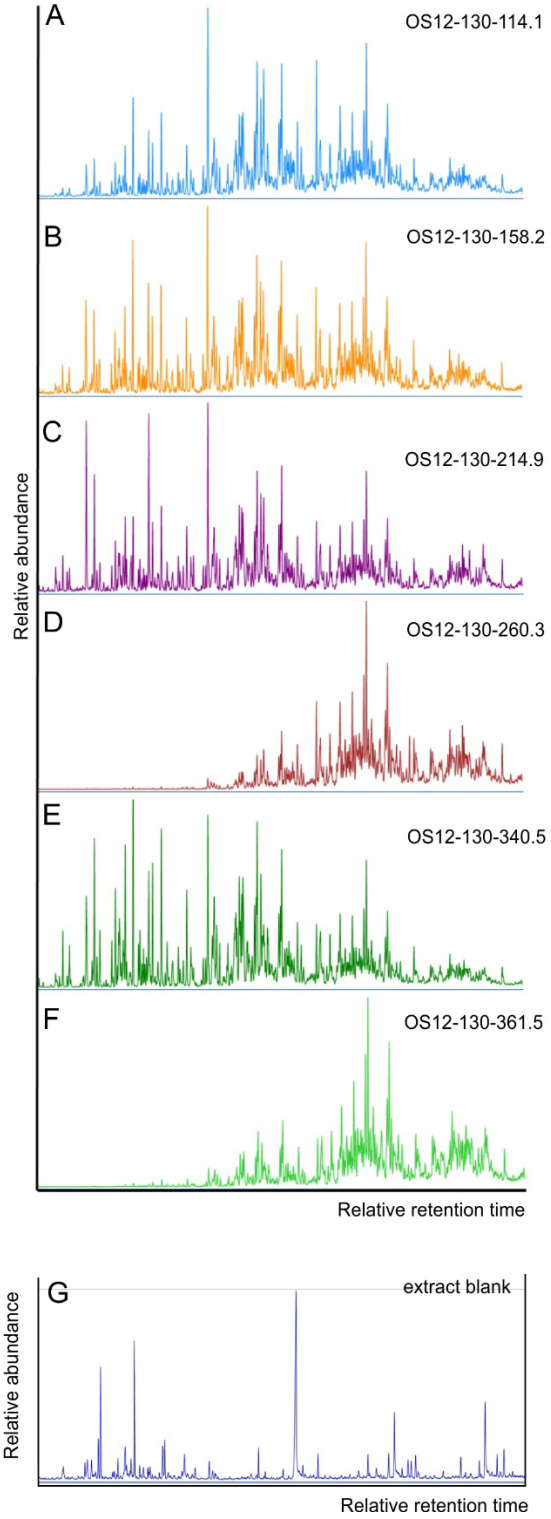

Figure 12. Fragmentograms of *m/z 57* for all the samples (A to F) and for the procedure blank (G).

Petrographic observations suggest that maturation occurred after the hydrocarbons has migrated and filled pores, which is in agreement with Time-temperature scenarios described in Pinet et al. (submitted) in which the maximum temperature recorded in borehole OS-12-130 has been reached either during tectonic burial or during the influx of hydrothermal fluids at *ca*. 74 Ma. This also indicates that hydrocarbon fluids did not transport gold at the deposit scale, an interpretation in agreement with the lack of hydrocarbons in fluid inclusions analyzed in late-mineralization calcite and fluorite (Pinet et al., submitted).

Relationship between organic matter and gold

At the scale of borehole OS-12-130, the relationship between TOC and Au (from assays on pluri-metric samples from the ATAC database) is unclear, and only two selected samples from high-grade (> 5 ppm Au) intervals have a significantly higher TOC values compared to their neighbours (Fig 13). The relationship between organic matter content and mineralization is better documented for selected samples. On the diagram TOC-Tl (the best pathfinder element for Au) organic-rich samples are significantly enriched in Tl (Fig. 14), suggesting higher-grade Au mineralization. A simple mass calculation assuming that the Conrad limestone was originally 69% calcite (average based on ATAC database and considering that all Ca is included in calcite) indicates that the removal of calcite through decarbonatization cannot fully explain the relationship between Tl and TOC, especially for medium grey to black rocks that are expected to have an originally lower calcite content than the limestone average. SEM-EDS data does not provide additional insights at the micro-scale on the spatial relationship between gold mineralization and organic matter. Interpretation of the high (several %) As content of bitumen filling pores (Fig. 9) remains hypothetical. If related to the main ore event, the lack of measurable gold could be related to its extremely fine size. If related to the almost Au-barren, late-stage of the mineralizing event characterized by the precipitation of late calcite and As-rich minerals (realgar, orpiment), the As content in pyrobitumen could record hydrothermal fluids cooler and more neutral (Hofstra and Cline, 2000) than Au-rich fluids.

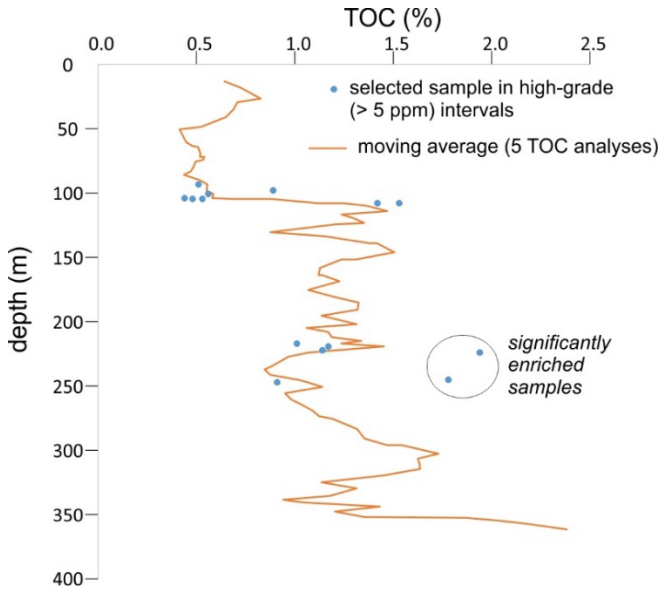

Figure 13. Comparison of TOC value in high grade intervals and moving average TOC value.

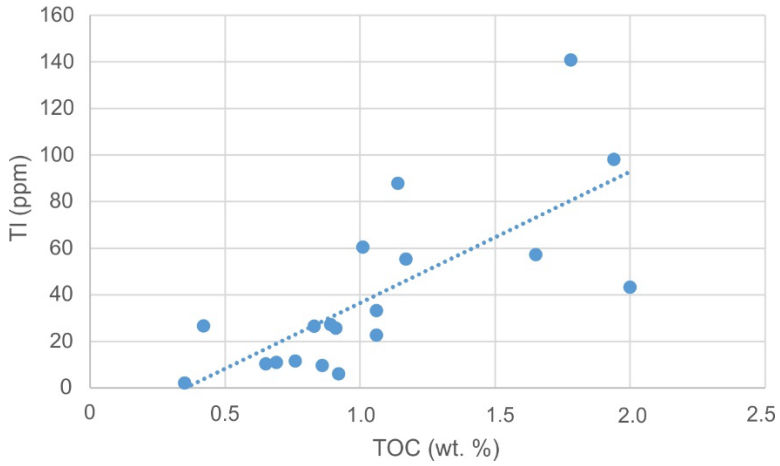

Figure 14. TOC versus Tl content plot. Comments in the text.

CONCLUSIONS

The main results of our detailed study of the relationship between organic matter and Carlin-type gold mineralization in Yukon are as follows:

1- The sedimentary succession hosting the Conrad deposit was relatively rich in organic matter, possibly related to Archea.
2- Pore and fracture filling bitumen is the dominant organic matter type in the studied samples. This type of bitumen results from the thermal cracking of liquid hydrocarbon emplaced before gold mineralization, indicating that hydrocarbon fluids cannot have served as an agent for gold transport. Bitumen disseminated in the rock or associated with stylolites are also documented.
3- The correlation between total organic carbon (TOC) and Tl (the best proxy for Au) for selected samples and the high As content of pyrobitumen filling pores may suggest a link between organic matter content and gold deposition, but this was not demonstrated at the microscale.
4- This study also demonstrates the difficulty to characterize the spatial relationship between 'invisible' gold and very small pyrobitumen particles at the microscale through EDS and LA-ICP-MS methods.

ACKNOWLEDGMENTS

Thanks to ATAC Resources for access to drill cores and data, and for logistical support and scientific input. Virginia Brake is acknowledged for her review and Patrick Mercier-Langevin for his continuous support. This is Yukon Geological Survey contribution No 060.

REFERENCES CITED

Beaton, N.I., 2015, Diagenetic controls on hydrothermal fluid flow in the Osiris, Isis and Isis East Carlin-type showings, Nadaleen trend, Yukon: M.Sc. thesis, Edmonton, Canada, The University of Alberta, 180 p.

Cline, J.S., Hofstra, A.H., Muntean, J.L., Tosdal, R.M., and Hickey, K.A., 2005, Carlin-type

gold deposits in Nevada: critical geologic characteristics and viable models: Economic Geology, v. 100, p. 451–484.

Dunham, R.J., 1962, Classification of carbonate rocks according to depositional texture, *in* Ham W.E. ed, Classification of Carbonate Rocks: American Association Petroleum Geologist Memoir, 1, 108–121.

Embry, A.F., and Klovan, J.E., 1971, A Late Devonian reef tract on Northeastern Banks Island, NWT: Bulletin Canadian Petroleum Geolologist, v. 19, p. 730–781.

Gribaldo, S, Brochier-Armanet, C., 2006, The origin and evolution of Archaea: a state of the art: Philosophical Transactions of the Royal Society B. v. 361, p. 1007-1022.

Hofstra, A.H., Cline J.S., 2000. Characteristics and models for Carlin-type gold deposits. Reviews in Economic Geology, v. 13, p. 163-220.

Hulen, J.B., Collister, J.W., 1999, The oil-bearing, Carlin-type gold deposits of Yankee Basin, Alligator Ridge district, Nevada: Economic Geology, v. 94, p. 1029-1050.

Ilchik, R.P., Brimhall, G.H., Schull, W.H., 1986, Hydrothermal maturation of indigeneous organic matter at the Alligator Ridge gold deposits, Nevada: Economic Geology, v. 81, p. 113-130.

Jarvie, D.M., Hill, R.J., Ruble, T.E., Pollastro, R.M., 2007, Unconcentional shale-gas systems: the Mississippian Barnett Shale of north-central Texas as one model for thermogenic shale-gas assessment: American Association Petroleum Geologists Bulletin, v. 91, p. 475-499.

Lafargue, E., Marquis, F., Pillot, D., 1998, Rock-Eval 6 applications in hydrocarbon exploration, production, and soil contamination studies: Revue de l'institut français du pétrole, v. 53, p. 421-437.

Landis, C.R., Castaño, 1995. Maturation and bulk chemical properties of a suite of solid hydrocarbons. Organic Geochemistry, v. 22, p. 137-149.

Large, R.R., Bull, S.W., Maslennikov, V.V., 2011, A carbonaceous sedimentary source-rock model for Carlin-type and orogenic gold deposits: Economic Geology, v. 106, p. 331-358.

Lawley, C.J.M., Petts, D.C., Jackson, S.E., Zagorevski, A., Graham Pearson, D., Kjarsgaard, B.A., Savard, D., Tschirhart, V.T., 2020, Precious metal mobility during serpentinization and breakdown of base metal sulphide: Lithos, 354-355, 105278, 16 p.

Meng, Q., Hooker, J., Cartwrigth, J., 2017, Early overpressuring in organic-rich shales during burial: evidence from fibrous calcite veins in the Lower Jurassic shales with beef member in the Western Basin, UK: Journal of Geological Society, v. 174, p. 869-882.

Moynihan, D., Strauss, J.V., Padget, C.D., and Nelson, L.L., 2019, Upper Windermere Supergroup and the transition from rifting to continent-margin sedimentation, Nadaleen River area, northern Canadian Cordillera: Geological Society of America Bulletin, v. 131, p. 1673–1701.

Muntean, J., 2018, The Carlin gold system: Applications to exploration in Nevada and beyond, in Muntean, J., ed., Diversity of Carlin-Style Gold Deposits: Society of Economic Geologists, Reviews in Economic Geology, v. 20, p. 39–88.

Muntean, J.L., Cline, J.S., Simon, A.C., and Longo, A.A., 2011, Magmatic-hydrothermal origin of Nevada's Carlin-type gold deposits: Nature Geoscience, v. 4, p. 122–127.

Pinet, N. and Sack, P., 2019, Macroscopic control on Carlin-type gold mineralization in north-central Yukon, in Rogers, N., ed., Targeted Geoscience Initiative: 2018 Report of Activities: Geological Survey of Canada, Open File 8549, p. 89–103.

Pinet, N., Sack, P., Mercier-Langevin, P., Colpron, M., Lavoie, D., Dubé, B., and Brake, V.I., 2020a, Neoproterozoic-hosted Carlin-type mineralization in central Yukon, part 1: regional- to prospect-scale geological controls: in Mercier-Langevin, P., Lawley, C.J.M., and Castonguay, S, eds., Targeted Geoscience Initiative 5: Contributions to the Understanding of Gold Systems: Geological Survey of Canada, Open File 8712, p. 281-297.

Pinet, N., Sack, P., Mercier-Langevin, P., Davis, W.E., Lavoie, D., Haeri-Ardakani, O., Dubé, B., Cline, J., Petts, D., Jautzy, J., Jackson, S.E., Percival, J.B., Savard, M.M., and Brake, V.I., 2020b, Neoproterozoic-hosted Carlin-

type mineralization in central Yukon, part 2: Mineralization, in Mercier-Langevin, P., Lawley, C.J.M., and Castonguay, S, eds., Targeted Geoscience Initiative 5: Contributions to the Understanding of Gold Systems: Geological Survey of Canada, Open File 8712, p. 299-314.

Pinet, N., Sack, P., Mercier-Langevin, P., Bécu, V., and Lauzière, K., 2021, Whole-rock geochemistry of samples Carlin-type gold zones, Nadaleen trend, Yukon. Geological Survey of Canada Open File 8767.

Pinet, N, Sack, P., Mercier-Langevin, P., Davis, W.J., Petts, D.C., Lavoie, D., Percival, J.B., Dubé, B., Colpron, M., Haeri-Ardakani, O., Brake, V.I., 2022a, Yukon's Carlin-type gold deposits (Rackla belt, Canada): main characteristics and new insights on alteration styles and geochemistry: Economic Geology, in press.

Pinet, N., Davis, W.E., Petts, D.C., Sack, P., Mercier-Langevin, P., Lavoie, D., and Jackson, S.J., 2022b. U-Pb vein calcite dating reveals the age of Carlin-type gold deposits of central Yukon, and a contemporaneity with a regional intrusion-related metallogenic event: Economic Geology, in press.

Pinet, N., Haeri-Ardakani, O., Jautzy, J., Savard, M. Sack, P., Colpron, M., Mercier-Langevin, P., submitted, Time-temperature frame of Carlin-type gold zones in Yukon, Canada: a multi-tool approach.

Ristorcelli, S., Ronning, P., Martin, C., and Christensen, O., 2018, Technical report and estimate of mineral resources for the Osiris project, Yukon, Canada (https://www.atacresources.com/assets/img/Osiris_Resource_Estimate_and_Technical_Report_2018.pdf)

Sack, P., Cline, J., Ren, M., Petts, D., and Pinet, N., 2019, Gold bearing pyrite in Carlin-type gold prospects of the Nadaleen trend, Yukon [abs.]: Geological Association of Canada annual meeting, Quebec, Canada, p. 169.

Steiner, A.P., and Hickey, K.A., 2019, Ore-stage calcite vein in the Carlin-type Au deposits of the Nadaleen trend, Yukon: a new addition to the geologist's tool-kit, Proceedings of the 15th SGA biennial meeting, Glasgow, August 2019, 4 p.

Steiner, A. P., Hickey, K.A., and Coulter, A., 2018, The structural framework for Carlin-type gold mineralization in the Nadaleen trend, Yukon: in MacFarlane, K.E., ed., Yukon Exploration and Geology 2017, Yukon Geological Survey, p. 139–149.

Tucker M.J., 2015, Geology, mineralization and geochronology of the Conrad zone Carlin-type prospect, east-central Yukon Territory, Canada: M.Sc. thesis, Vancouver, Canada, The University of British Columbia, 160 p.

Tucker, M.J., Lane, J.C., and Hart, C.J.R., 2018, Overview of Carlin-type prospects of the Nadaleen trend: a Yukon analogue to Carlin-type gold mineralization of the Great Basin, in Muntean, J., ed., Diversity of Carlin-style gold deposits: Society of Economic Geologists, Reviews in Economic Geology, v. 20. p. 235–256.

Williams-Jones, A.E., Bowell, R.J., Migdisov, A., 2009, Gold in solution: Elements, v. 5, p. 281-287.

Wirth, R., Reid, D., and Schreiber, A., 2013, Nanometer-sized platinum-group minerals (PGM) in base metal sulphides: new evidence for an orthomagmatic origin of the Merensky reef PGE ore deposit, Bushveld Complex, South Africa: The Canadian Mineralogist, v. 51, p. 143-155.